ROYAL SOCIETY OF CHEMISTRY

PAPER

Check for updates

Sensitive particle shape dependence of growth-induced mesoscale nematic structure†

Jonas Isensee [ID] [ab] and Philip Bittihn [ID] *[ab]

Directed growth, anisotropic cell shapes, and confinement drive self-organization in multicellular systems. We investigate the influence of particle shape on the distribution and dynamics of nematic microdomains in a minimal *in silico* model of proliferating, sterically interacting particles, akin to colonies of rod-shaped bacteria. By introducing continuously tuneable tip variations around a common rod shape with spherical caps, we find that subtle changes significantly impact the emergent dynamics, leading to distinct patterns of microdomain formation and stability. Our analysis reveals separate effects of particle shape and aspect ratio, as well as a transition from exponential to scale-free size distributions, which we recapitulate using an effective master equation model. This allows us to relate differences in microdomain size distributions to different physical mechanisms of microdomain breakup. Our results thereby contribute to the characterization of the effective dynamics in growing aggregates at large and intermediate length scales and the microscopic properties that control it. This could be relevant both for biological self-organization and design strategies for future artificial systems.

1 Introduction

Ensembles of passive particles can be grouped and characterized as classical phases of matter such as solids, fluids or glasses. In active matter, the particles possess some form of inherent activity that drives the behaviour. Depending on the form and strength of activity, the resulting dynamic processes may cause aggregates to resemble classical phases[1–4] or to take on new forms such as self-propelled[5] or rotating aggregates.[6] One type of activity that is not only highly relevant in biology but can also crucially influence the properties of soft matter is growth combined with cell division.[7–9] Energy is injected in the form of microscopic building materials to permit assembly, leading to self-crowding induced confinement that can mediate self-organisation.[10] Example systems are cells replicating within tissues, bacteria or, in the future, even proliferating synthetic droplets for which only parts of the required mechanisms have been successfully implemented so far.[11–13]

What makes growing active matter particularly interesting is that it violates some of the most fundamental symmetries of classical matter, namely mass and number conservation. Systems where mass is conserved but the cell number increases[14] include the development of embryos inside hard eggshells. Due to the importance of embryonic development in understanding the origins of life, a multitude of experimental and theoretical studies are contributing at various levels, identifying mechanisms of shape formation through morphogen gradients,[15,16] or through inference and impact of mechanical stresses,[17–21] to only name a few. Different dynamics emerge from growth when the symmetries are broken locally but conserved on average. In a tissue of a single species of cells one can consider homeostatic turnover and when different cell types are introduced manually or by random mutation, competition for shared space may emerge, where different mechanical mechanisms have been investigating, including differing division rates,[22] homeostatic pressure,[23] and competition *via* passive remnants of cells.[24]

Thirdly, when mass and number conservation are fully broken, large-scale expansion is an inevitable consequence. Cells growing in volume can expand isotropically, however (binary) division naturally requires a symmetry breaking and therefore some anisotropy on the particle scale.[25] In fact, many microorganisms in nature such as bacteria expend energy to maintain their preferred shapes against external influences.[26] Biological mechanisms to achieve this include the production and localization of curvature proteins that deform the cell membrane[27,28] in a balance with surface tension.[29] On the inside, cells can have cytoskeletal dynamics controlled by motor proteins acting on a scaffold of actin filaments, microtubules, and intermediate filaments to internally support shape changes, and on the outside active force generation through substrate adhesion and intracellular forces

a Max Planck Institute for Dynamics and Self-Organization, Göttingen, Germany.
 E-mail: philip.bittihn@ds.mpg.de
b Institute for the Dynamics of Complex Systems, University of Göttingen, Göttingen, Germany

and interactions with the extracellular matrix is used to build cell shapes.[26]

More recently, experimental studies have also linked cell shapes to competitive advantages[30,31] and irrespective of the concrete mechanisms,[32] actively maintained shapes combined with growth and division of the constituent cells are known to cause striking emergent behaviour. Studying the most commonly found explicitly maintained shape, the rod with circular caps, previous studies have explored the orientational alignment dynamics in experiments with, *e.g.*, *E. coli* bacteria[33–38] or *Bacillus subtilis*[39,40] and also using particle-based numerical simulations. It has been shown that the alignment of such growing rods is on average determined by the growth-generated expansion flow field and that the strength of ordering further depends on the division aspect ratio of the rods themselves: When placed into micro-fluidic channels both in simulation and experiment,[34,41,42] one finds alignment along the channel and with sufficiently large division aspect, the dynamics may even produce columnar tip–tip patterns toward the channel outlet. This transition to perfect order was found to be accompanied by a peculiar change in observed stress mechanics:[42] while partially ordered systems always feature an excess stress between walls and orthogonal to alignment as discussed in ref. 43, the opposite is observed in the columnar state with important implications for the stability of highly aligned microdomains even under excess compressive stress in the direction of cell orientation. To some extent, this motivates why microdomains are observed in freely expanding circular colonies in the first place.[33,36]

Despite the numerous experimental and numerical works, finding the most appropriate effective description is still a topic being actively researched.[36,43–47] As the rods have a 180° rotation symmetry, effective descriptions fall into the class of nematic theories with a range of successful models on liquid crystal physics to build upon.[48–53] Consequently, the extant continuum models of nematic growing matter use a Q-tensor formulation with spontaneous order and Oseen–Franck elasticity terms.[54,55] For example filamentous active nematics[56,57] and bending rod-shaped bacteria[58,59] feature smooth nematic order parameter fields that can be studied using elastic constants and topological defects. However, an important difference of the rigid growing rods from the typical application of classical nematic theories is that the finite granularity of growing rods is crucial. Orientational alignment is mediated by concrete pressure and shape-dependent particle–particle interactions rather than a background fluid and means that the energetic penalty of disalignment remains finite even for diverging gradients of the nematic director field. This moves the dynamics to a different regime where the striking features of the orientational field are highly ordered microdomains separated by sharp disclination lines.

In this work we seek to provide another puzzle piece toward a better understanding of this regime and in particular how it depends of the microscopic shape details of the particles. On top of the division aspect of rods, we introduce a shape parameter called *pointiness* that allows a continuous variation

of the tip shape, enabling us to discuss the robustness of the dynamics to small deviations from the simple circle-cap rod shape and also explore the behaviour further from biologically relevant shapes. Using a first-principles mathematical model, we illustrate how the distribution of observed microdomain sizes can be mapped to effective stability properties that hint at distinct breakup mechanisms for microdomains. Beyond informing the theoretical understanding of the emergent dynamics, these results could have applications in future design of artificial materials by tuning the shapes of microscopic building blocks using synthetic scaffolds and curvature proteins during self-assembly.

2 Methods

2.1 Agent-based modeling

For our numerical simulations, we consider agents of various shapes that grow in length and divide. Each agent occupies the space defined by its shape and the only interaction between agents is volume exclusion. This is realized through the introduction of surface-normal repulsion forces whenever agents overlap as is illustrated in Fig. 1A. The precise definition of the repulsion force depends on the shape details and is given in Section S1 (ESI†).

Simulations are set in the over-damped limit. This makes particle velocity $\mathbf{v}_i = \mu_i \mathbf{F}_i$ instantaneously defined by the sum of all pairwise interaction forces $\mathbf{F}_i$ and the particle size-
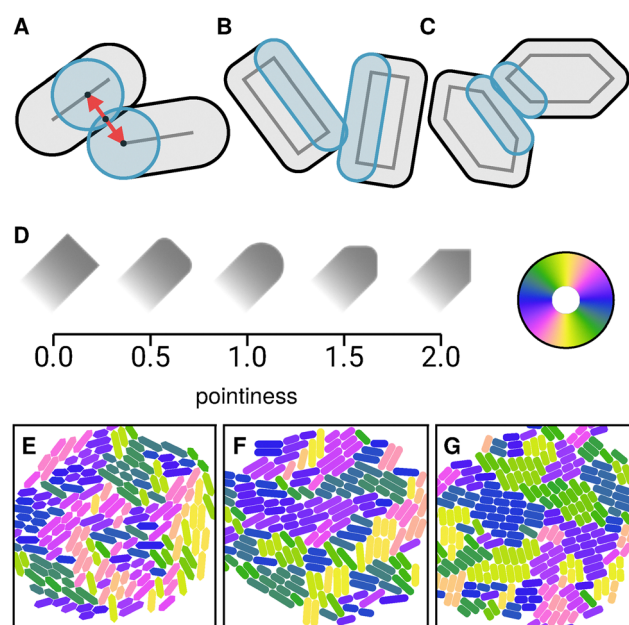

Fig. 1 (A) Illustrations of normal repulsion force between two touching rods, (B) rounded rectangle rods, and (C) pointy rods. In each case the interaction is implemented using the closest-point method based on line segments. (D) The shape parameter pointiness $\mathscr{P}$ is used to parameterize the tip-shape modification. (E–G) Snapshots of simulations at an early stage with parameters $(a_d, \mathscr{P}) = (4,1.8),(4,1),(3,0.8)$ in order with coloring to emphasize (nematic) orientations as defined in the color wheel.

dependent mobility tensor μ_i as explained in more detail in Section S1 (ESI†).

Our implementation of these models is available online as part of our in-house developed open-source framework for agent-based simulations of interacting particles InPartS.[60]

2.2 Agent shapes

We define a set of particle models with the capacity for growth and division but varying shape details. The most common model for growing nematic bacteria is the rod model.[33,34,36,42,44,47] There, particles consist of a fixed-width body with half-circle caps at opposing ends as shown in Fig. 1A. A necessary requirement for all models with (indefinite) growth and binary divisions is that particle volume approximately doubles during its lifetime. In the case of the rod model, the width stays fixed while the body length between the caps increases to reach its division aspect a_d at which point the particle instantaneously divides in the middle to produce two new particles. Inspired by research on formation of smectics in liquid nematic crystals[61] we define a generalization of the rod model with a tip shape that can be continuously varied from flat to pointy as shown in Fig. 1D with a control parameter pointiness $\mathcal{P}$. The pointiness takes values in the open interval $\mathcal{P} \in (0, 2)$ where a value of 1 recovers the original rod model. For $\mathcal{P} \leq 1$ the outline becomes a rounded rectangle (Fig. 1B) with corner radius $r_c = R\mathcal{P}$ with R the cap radius of the original rod shape. For $\mathcal{P} \geq 1$, the agents gain a (rounded) triangular cap (Fig. 1C) with corner radius $r_c = R(2 - \mathcal{P})$ and side lengths scaled to preserve the bounding box. Note that both outer limits of the pointiness, $\mathcal{P} = 1$ and $\mathcal{P} = 2$, lead to non-rounded actual corners in the model that are not studied as part of this work. Further details on our modeling approach are presented in Section S1 (ESI†).

2.3 Setup

A key challenge in characterizing emergent dynamics in models describing growth processes is to correctly identify or separate the emergent bulk dynamics from boundary effects (*e.g.* confinement)[42] and history dependence (initial conditions).

Similar to previous research[33,36] we work without explicit confinement and consider a freely‡ expanding aggregate which, independent of the precise initial condition, quickly takes on a circular disk shape. To also ensure access to stationary dynamics, we implement an indiscriminate removal of particles reaching a specified radial distance from the domain center. For length scale comparisons across parameter variations, we define the area of newly created agents (approximated by their bounding rectangle) as a unit area. Unless specified otherwise, the disk domains have a diameter of 150 allowing for $\approx 10^4$ agents at a time. Example configurations found in an early stage of the evolution are shown in Fig. 1E–G and snapshots of full-size simulations are displayed in Fig. 2A.

---

‡ Motion is opposed by surface friction. Any expansion flow needs to be continuously driven by an internal pressure buildup.
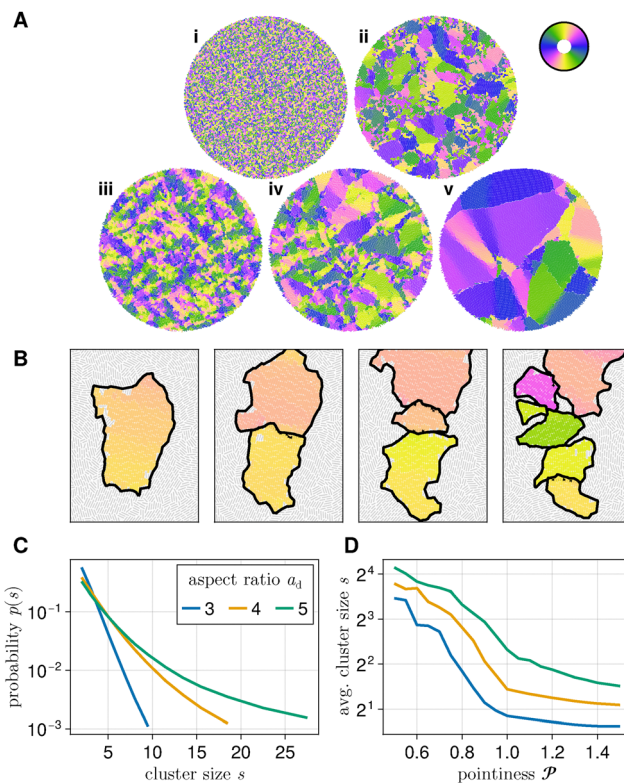

Fig. 2 (A) Example snapshots for varied agent shapes. The pointiness $\mathcal{P}$ has values (1, 1/2, 3/2, 1, 1/2) in I–V and the division aspect a_d are 2 in I & II and 5 in III–V. The full time evolution of these examples is animated in the ESI† Movies 1–5. (B) A growing and breaking microdomain is tracked over time with $\Delta t = 0.5$ between snapshots. (C) Cluster size distributions $p(s)$ for rods with division aspect $a_d = 3, 4$, and 5. (D) Average cluster size s for varied pointiness $\mathcal{P}$ and division aspect a_d.

3 Results

The simulated dynamics spontaneously produce patches of highly aligned rods depending on division aspect and tip shape. Examples of different combinations are shown in Fig. 2A. While no average global nematic order develops, the mesoscopic nematic structures show marked differences across the parameter space: Short regular $\mathcal{P} = 1$ rods (I) form no structures but short rectangular $\mathcal{P} = 0.5$ agents (II) do form structures similar to much longer rods (IV) with $\mathcal{P} = 1$. Increased pointiness reduces the size of emergent structures at large division aspect (III) while the combination of low pointiness and large aspect yields the largest microdomains (V).

3.1 Clustering

As mentioned above and visually evident from the snapshots in Fig. 2A, the agents group into highly aligned microdomains of characteristic parameter-dependent size. To identify clusters, we construct an undirected graph with particles as vertices and add edges between interacting particle pairs whose orientations are approximately equal. A standard connected-component analysis then yields the assignment into microdomains. For the original rod model a similar analysis was done by You *et al.*[33] In general, the results of any clustering analysis will depend crucially on the

choice of tolerance. However, separately testing the effects of tolerance (done in Fig. S6, ESI†) and subsequently keeping it constant for further analysis still allows for many conclusions to be made. All analyses shown here use a tolerance of 0.02 rad $\approx$ 1 deg. An example of a microdomain growing over time and subsequently breaking up into smaller pieces is shown in Fig. 2B. While the clustering works on instantaneous configurations only, the continuity was recovered by tracking the constituent cells and their descendants in time.

Probability distributions of cluster sizes are shown in Fig. 2C for a range of parameters. For agents that form relatively small clusters (here $a_d = 3$) we find approximately exponentially distributed sizes. This is in line with the results by You et al.[33] Interestingly, for large division aspect a_d the scaling gains heavy tails resembling a power law distribution and, as will be shown below, the same is true for low pointiness values.

To summarize the distributions, Fig. 2D shows the mean cluster size as a function of pointiness for division aspect $a_d = 3$, 4, and 5. The average cluster size increases the more boxy agents get ($\mathscr{P} \to 0$) leading to significant cluster formation even for the shortest ($a_d = 3$) agents. Pointy tip shapes inhibit the formation of large clusters.

Pursuing a better understanding of the mesoscopic dynamics, we will point out important aspects of the emergent size distributions.

3.2 General properties

In a first step, we view radially resolved stationary size distributions computed using the clustering algorithm introduced above. Up to some boundary region, the size distribution is uniform in space as shown in Fig. 3A where the probabilities of different size ranges are displayed as a function of the relative radial position. The radial position of each cluster is determined as its centroid, and consequently the center of large clusters can never reach the outer cutoff. Beyond this geometric constraint, the distribution is not only homogeneous in space but also becomes stationary after a short transient at the largest cluster sizes. This is visualized in Fig. 3B where a set of subsequent instantaneous size distributions is computed from 10 independently initialized developing colonies. Initially, only very few agents are present but the domain becomes fully filled at time $t \approx 12$. Up until that point, one observes a preference for tangential alignment of cells positioned at the periphery of the expanding colony. This was previously reported in ref. 36 and we reproduce this finding in Section S4 (ESI†). Once the domain is fully covered and particles begin to flow out the domain perimeter, this boundary effect vanishes, and the microdomain size distribution quickly converges, with the largest cluster sizes being the last to fully saturate (Fig. 3B).

When changing the overall system size, we find that the power-law type distribution tails, where present, scale accordingly. As a consequence, the average size of observed clusters remains approximately constant for division aspect $a_d = 3$ and increases with domain size for higher division aspects as shown in Fig. 3C. The general shape of the distributions of the microdomain size s shown in Fig. 3D on the other hand
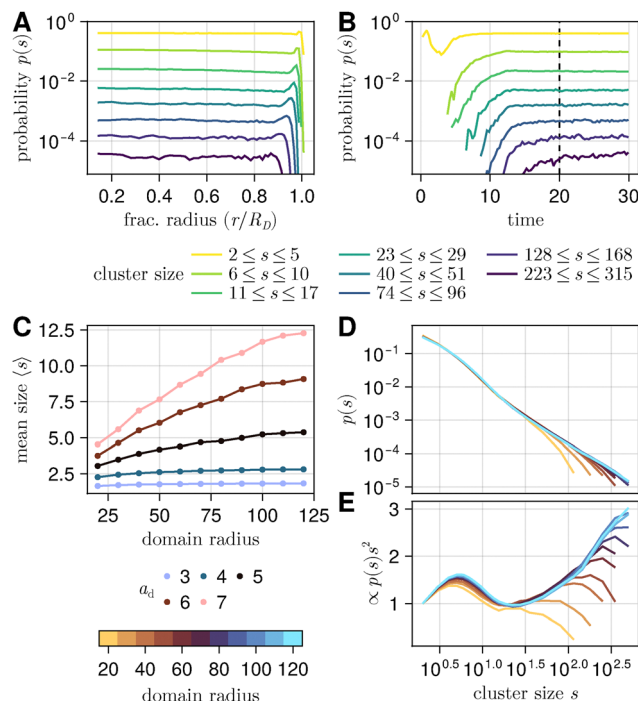

Fig. 3 Size distribution properties of rodcells. (A) Cluster size distribution $p(s)$ as a function of radial position for division aspect $a_d = 5$ discretized on colorcoded intervals. (B) Cluster size distribution over time with $a_d = 5$. (C) Average cluster size for varied division aspect a_d and domain size. (D) Size distributions $p(s)$ for varied domain size at $a_d = 6$, and (E) also shown multiplied by s^2 to emphasize changes in scaling and the distribution tails.

remains similar. Only the cut-off beyond the power-law-like tails moves to larger sizes. To further emphasize the variations, Fig. 3E displays the same data rescaled by s^2 and normalized by the left-most values. A positive slope indicates a local decay rate of the size distribution that is slower than $\propto s^{-2}$ while for negative slopes it is faster. Comparing this to the log–log data above, we identify the first local maximum with the exponential decay at small sizes and what follows is a power-law type decay with exponent > -2 ended by a domain size dependent cut-off.

3.3 Shape variation

With these general observations in hand, we can now turn to the parameter dependence of these distributions in more detail. Fig. 4A shows the measured sizes for $\mathscr{P} = 1$ rods with division aspects a_d varied from 2 to 7. To visually emphasize the differences between various distributions $p(s)$ we additionally display $p(s)s^2/Z$ in Fig. 4B with constant scaling $Z = p(s_{min})s_{min}^2$ and the quadratic size s^2 to bring the distribution tails into focus. For all parameters, the distributions are well approximated by the sum of an exponential decay and a power law

$$p(s) = c_1 e^{-s/\gamma_1} + c_2 s^{-\gamma_2} \tag{1}$$

except for the limits of the observed sizes where finite-size and finite-number effects dominate.

Short particles predominantly show exponential decay. The fit parameters in Fig. 4C for the power-law term yield large prefactors but large decay exponents as well, indicating only small
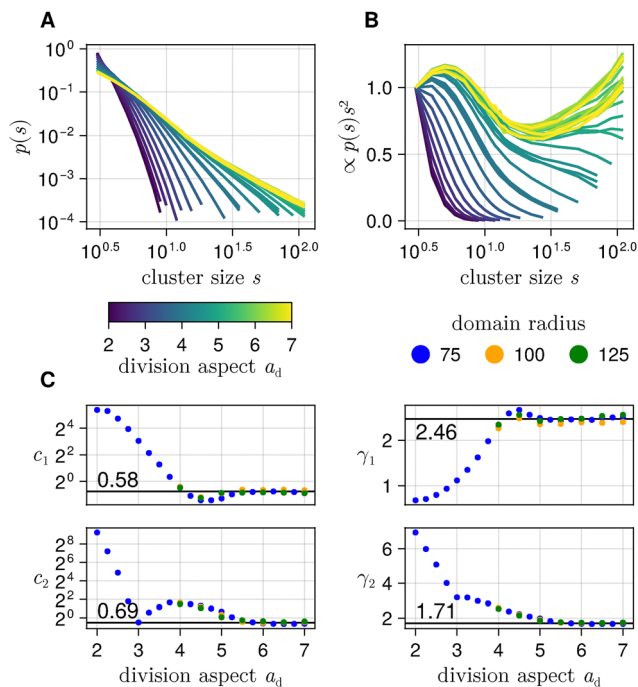
Fig. 4 (A) Size distributions $p(s)$ for rods with varied division aspect a_d. (B) Distributions multiplied by s^2 and normalized to give 1 at the left-most data point to emphasize the distribution tails. (C) Fit parameters of eqn (1) to the data shown in Fig. 4A. Side-by-side plots of data and fitted function can be found in Fig. S7 (ESI†).

Fig. 5 Cluster size distributions $p(s)$ for varied pointiness $\mathscr{P}$. (A) Distributions multiplied for pointiness $\mathscr{P} \in [0.5, 1.1.5]$ split into separate panels. Coloring indicates division aspect a_d. (B) Distribution tail weight represented as the size s at which the probability density crosses $p(s) = 10^{-4}$.

corrections at the smallest sizes. An increase in division aspect a_d first increases the decay length scale γ_1 but also drives a transition towards power-law scaling. With increasing division aspect a_d, both the exponential decay length γ_1 and the power law exponent γ_2 move towards longer distribution tails. Interestingly, this process saturates at division aspect $a_\mathrm{d} \approx 5$ with the distributions seemingly converging both in length scale and amplitudes. This is invariant under changes of the domain size, in line with results from above.

Similar trends can be observed in Fig. 5 where both division aspect a_d and pointiness $\mathscr{P}$ are varied. While pointy tip shapes $\mathscr{P} > 1$ inhibit the formation of large clusters, an increased division aspect still drives the distribution toward power-law tails. For sufficiently low pointiness (e.g. $\mathscr{P} = 0.5$), the distributions become heavy-tailed at all division aspects. The precise distribution shapes differ slightly from those of regular rods and are not described as well by eqn (1). Instead, this trend is summarized in Fig. 5B where tail weight is approximated using the cluster size s for which $p(s) = 10^{-4}$ is reached. Parameters where exponential decay dominates appear dark, as the target probability is reached for comparatively small cluster sizes, while increased division aspect or lower pointiness move the target probability toward larger sizes. A non-obvious result is that the largest clusters are found in the bottom left corner of Fig. 5B (for low pointiness and small division aspect) rather than in the top left corner. This indicates the existence of an optimal trade-off between maximized division aspect and absolute width of the tips. These are not independent, as the average area is conserved.
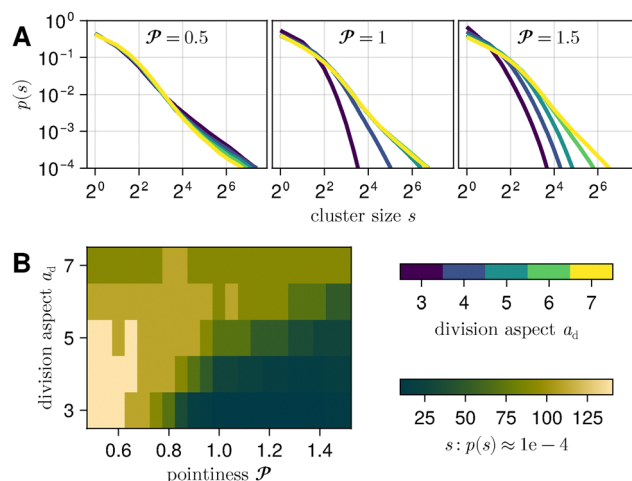
3.4 A master equation for microdomains

In the previous section we found that the emergent dynamics yield a stationary distribution of microdomain sizes. Importantly, the shape of the distributions varies from exponential to predominantly power-law distributed. To better understand the implications of this change, we neglect all spatial dynamics and set up a master equation for the likelihood of finding microdomains of different sizes. Microdomains consist of growing and dividing agents, leading to exponential growth of each microdomain. When considering the area fraction $A(s,t)\mathrm{d}s \propto sp(s,t)\mathrm{d}s$ of clusters of size s, time t, and number distribution $p(s,t)$, growth can be expressed as an advection term with a velocity s in size space due to the exponential nature of growth. Here, time is rescaled to absorb the growth-rate dependence.

The only additional process allowed for this calculation is microdomain breakup. When numerically determining the time evolution of microdomains from particle simulations, we observe a range of different breakup scenarios owing to the finite granularity of the particles, as illustrated in Fig. 2B. Here, we try to describe the fundamental aspect of the dynamics and therefore consider the most simple and tractable mechanism that is breakup into equal halves with a size-dependent rate $\beta(s)$. In the area fraction description, this turns into a non-local coupling and the full equation yields

$$\partial_t A(s) + \partial_s(sA(s)) = -\beta(s)A(s) + 2\beta(2s)A(2s) \quad (2)$$

where the last term is evaluated at $2s$ and also has a factor 2 from the measure at $2s$. Due to chosen units for $A(s,t)$ no additional factors are needed and the distribution stays normalized automatically.

Both the rate $\beta(s)$ and distribution $A(s,t)$ are *a priori* unknown. However, we are specifically interested in understanding the dynamics involved in producing stationary exponential and power-law (number) distributions. Assuming a specific stationary $A(s)$, we can solve for the corresponding
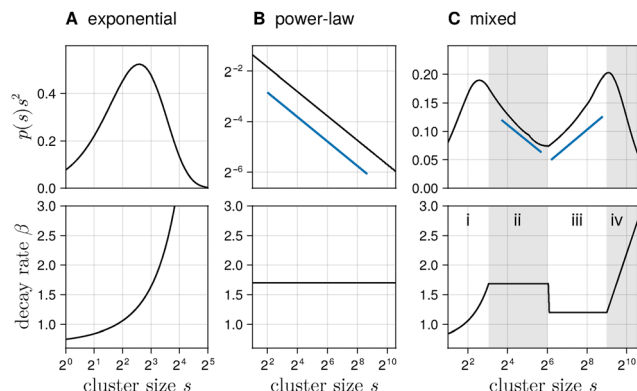
Fig. 6 Numerical steady state solutions of eqn (2) for varied prescribed decay rate functions $\beta(s)$ in panels (A), (B), and (C). Solutions, scaled with the squared size s^2, are shown above their corresponding β. Roman numerals are placed in Fig. 6C to label the (i) exponential, (ii) steep power-law, (iii) shallow power-law, (iv) long-range cut-off, regimes. Expected power-law scaling computed using eqn (4) is highlighted in blue.

$\beta(s)$. For an exponential number density we require $A(s) \propto s e^{-s/a}$. Plugging this into eqn (2) yields

$$0 = -2 + \frac{s}{a} - \beta(s) + 4\beta(2s)e^{-s/a}$$

and is solved by

$$\beta(s) = \sum_{n=1}^{\infty} \left(\frac{2}{4^n} - \frac{s}{8^n a} \right) \exp\left(\frac{s}{a}\left(1 - \frac{1}{2^n}\right) \right) \qquad (3)$$

as derived in Section S3 (ESI†). In contrast, requiring a number density with power-law decay $A(s) \propto s^{\gamma+1}$ leads to

$$0 = -(\gamma + 2) - \beta(s) + \beta(2s)2^{\gamma+2}$$

and is solved by the constant decay rate

$$\beta(s) \equiv \beta = \frac{\gamma + 2}{2^{\gamma+2} - 1}. \qquad (4)$$

In the former case of an exponential number distribution, we find a size-dependent decay rate. It is visualized in Fig. 6A and features an increasingly large decay rate beyond the characteristic size a. This is in line with the notion that microdomains beyond their stable size eventually buckle under their self-generated load.

Power-law distributions, shown in Fig. 6B, on the other hand yield a constant decay rate independent of cluster size. This indicates that the buckling instability is no longer the dominant process and, instead, the dynamics are better described by breakup through stochastic input from the surrounding bath (of other microdomains).

An interesting observation in the data gathered from agent-based simulations is the bimodal nature of $p(s)s^2$ in, e.g., Fig. 3D. By definition, this means that the local decay exponent varies above and below -2. In the context of the decay model, this can be understood as an effective size-dependent variation in stability. To emphasize this point, Fig. 6A shows a hand-crafted decay rate function $\beta(s)$. It consists of an exponential region (i, compare Fig. 6A) for small sizes, two power-law

regimes (ii & iii) with varied expected exponent and a large size cut-off in (iv). The analytically expected power-law scalings computed using eqn (4) were added in blue in both Fig. 6B and C.

At small cluster sizes, there is a natural limit imposed by the agent-based simulations that no clusters with fractional cell numbers may exist. The largest possible clusters are bounded by the finite simulation domain, however, in practice, no such clusters are ever observed. This imposes a bound on the valid regime of power-law decay exponents. The parameter fits in Fig. 4 revealed an asymptotic exponent $\gamma_2 < 2$. If this scaling continued to infinite sizes, the average size would diverge and numerical observations should never reveal more than a single globally aligned patch. As this is clearly not the case, an exponent $\gamma_2 < 2$ must be accompanied by a large size cut-off, as also added in Fig. 6C.

4 Conclusion

Our work shows that subtle differences in similarly spirited systems can yield surprising differences in the emergent dynamics. Modifying the tip shape to be flat-spotted or more strongly pointed has a strong impact on the stability of tip–tip interactions that regularly occur after cell divisions and are a crucial ingredient in microdomain formation. This extends the observations of Boyer et al.[34] who described the *buckling instability* of ordered bacterial colonies due to circular tip interactions.

Lowering the pointiness and hence turning the rods into a rounded rectangle shape allows the agents to form long identically aligned columns prior to buckling. This phenomenon enables the formation of large microdomains even with division aspects that normally do not exhibit meaningful self-organization.

Increased pointiness on the other hand inhibits the formation of large clusters. However, it enables an additional efficient packing configuration where neighboring rows of aligned agents are displaced by half a particle width. This kind of behaviour has also been reported by King & Kamien[61] and anecdotal evidence of this in our simulations is shown in Fig. S5 (ESI†). We found that the right combinations of tip-shape and division aspect can stabilize alignment to effectively inhibit self-buckling, leading to a change in the size distributions toward power-law as argued in Section 3.4. Beyond this point, only the total domain size appears to change the emergent distributions by setting a cut-off for the large-size power-law scaling. This is a non-trivial observation. Despite all interactions in the model being local pairwise repulsion forces, the domain boundaries manage to control a spatially homogeneous microdomain size distribution. This rules out the simplest hypothesis that the total pressure field might be the sole mediator and more analyses possibly on varying geometries might be able to determine the mediating field.

In previous work,[33] You et al. discovered that the characteristic length scale of microdomain size distributions can be

described by the ratio of an emergent bending stiffness of the ordered phase and an active stress extracted from an anisotropic average co-rotational stress tensor. This is different in language but similar in spirit to the stability of ordered domains under anisotropic stress discussed in ref. 42. Notably, according to their analysis in ref. 33, both emergent quantities are proportional to the excess density, leaving the length scale constant. This is in agreement with our observation that the distribution of microdomain sizes is constant in the bulk and does not change with radial position, though it is also incomplete, as we find the mean cluster size to increase with simulation domain size. Reversing the relation of microdomain sizes and bending stiffness, we conclude that an increased pointiness $\mathscr{P} > 1$ should reduce the material stiffness, while rounded rectangular $\mathscr{P} < 1$ particles would produce an increased stiffness. Despite the appeal of a single parameter dependent bending stiffness that could be related to the Oseen–Franck constants of a nematic continuum theory, it is important to point out that the measured stiffnesses are only meaningfully defined for the perfectly ordered state found within microdomains. At interfaces between microdomains, one finds sharp disclination lines at the particle length scale, a feature that is obvious from the particle simulations but difficult to capture in a continuum formulation based on stiffness constants, as it would require highly non-linear terms. However, this is where this work on shape variations can lend inspiration for future work. Particles within growing colonies experience a grow-generated stress and all particle motion follows stress gradients to reduce it. A local pathway of reducing isotropic pressure is through the reorientation of particles to maximize the fraction of occupied space. Keeping in mind the continuous growth and resulting polydispersity of particles, it becomes clear that this should on average favour the nematically aligned state. Furthermore, this process crucially depends on the particle shapes. Rounded and low aspect ratio shapes rotate easily, but rectangular ($\mathscr{P} \to 0$) particles can pack the space most efficiently when ordered. Coupling the material density to nematic order was already mentioned in ref. 35 and we show evidence of shape-dependent packing fractions in Section S4 (ESI†). Viewing alignment from this perspective then allows us to conclude that the size distribution of microdomains should naturally depend on shape parameters like the division aspect and the pointiness as they tune the geometric stability of the nematically ordered state. This brings us back to the microdomain master equation model. Neglecting all spatial dynamics and considering divisions into equal halves with a size-dependent division rate, we formulated a mathematical model that is analytically tractable and still captures the essence of the much more complex spatio-temporal particle dynamics. Calculations based on these assumptions then allowed us to interpret the changing size distribution shapes as variations in mechanical stability, thus complementing the above discussion on the microscopic origins of stability of the ordered state in microdomains.

Due to our simple modeling assumptions, the phenomenology observed in this work can only scratch the surface of the dynamics possible in experimental analogues. However, this approach allowed us to connect the striking dynamics of microdomains with distinct disclination and specific length scales to the microscopic shape details of the constituent particles. The results thus contribute to a more comprehensive understanding of the effective processes involved in the growth and division of rigid rod-shaped particles and may also provide useful context in future designs of self-assembling synthetic materials.

Data availability

Simulation codes used for this study were built on top of the open-source framework InPartS.jl[60] with analyses conducted using the Julia programming language[62] and visualizations using Makie.jl.[63] Code to simulate the agent-based models including interactive visualization and the numerical solver for the master equation model can be accessed at **https://hdl. handle.net/21.11101/0000-0007-FE61-E**.

Conflicts of interest

There are no conflicts to declare.

Acknowledgements

Notes and references

1 T. B. Liverpool, A. C. Maggs and A. Ajdari, *Phys. Rev. Lett.*, 2001, **86**, 4171–4174.
2 Y. Hatwalne, S. Ramaswamy, M. Rao and R. A. Simha, *Phys. Rev. Lett.*, 2004, **92**, 118101.
3 L. Berthier and J. Kurchan, *Nat. Phys.*, 2013, **9**, 310–314.
4 L. M. C. Janssen, *J. Phys.: Condens. Matter*, 2019, **31**, 503002.
5 T. Vicsek, A. Czirók, E. Ben-Jacob, I. Cohen and O. Shochet, *Phys. Rev. Lett.*, 1995, **75**, 1226–1229.
6 T. H. Tan, A. Mietke, J. Li, Y. Chen, H. Higinbotham, P. J. Foster, S. Gokhale, J. Dunkel and N. Fakhri, *Nature*, 2022, **607**, 287–293.
7 J. Ranft, M. Basan, J. Elgeti, J.-F. Joanny, J. Prost and F. Jülicher, *Proc. Natl. Acad. Sci. U. S. A.*, 2010, **107**, 20863–20868.
8 A. Gelimson and R. Golestanian, *Phys. Rev. Lett.*, 2015, **114**, 028101.
9 O. Hallatschek, S. S. Datta, K. Drescher, J. Dunkel, J. Elgeti, B. Waclaw and N. S. Wingreen, *Nat. Rev. Phys.*, 2023, **5**, 407–419.

10 N. A. M. Araújo, L. M. C. Janssen, T. Barois, G. Boffetta, I. Cohen, A. Corbetta, O. Dauchot, M. Dijkstra, W. M. Durham, A. Dussutour, S. Garnier, H. Gelderblom, R. Golestanian, L. Isa, G. H. Koenderink, H. Löwen, R. Metzler, M. Polin, C. P. Royall, A. Šarić, A. Sengupta, C. Sykes, V. Trianni, I. Tuval, N. Vogel, J. M. Yeomans, I. Zuriguel, A. Marin and G. Volpe, *Soft Matter*, 2023, **19**, 1695–1704.

11 A. A. Cheng and T. K. Lu, *Annu. Rev. Biomed. Eng.*, 2012, **14**, 155–178.

12 C. Guindani, L. C. d Silva, S. Cao, T. Ivanov and K. Landfester, *Angew. Chem., Int. Ed.*, 2022, **134**, e202110855.

13 Y. Dreher, K. Jahnke, M. Schröter and K. Göpfrich, *Nano Lett.*, 2021, **21**, 5952–5957.

14 S. R. Lish, L. Hupe, R. Golestanian and P. Bittihn, Isovolumetric Dividing Active Matter, *arXiv*, 2024, preprint, arXiv:2409.20481, DOI: 10.48550/arXiv.2409.20481.

15 A. M. Turing, *Philos. Trans. R. Soc.*, 1952, **237**, 37–72.

16 S. V. Bryant and D. M. Gardiner, *Regeneration*, 2016, **3**, 103–122.

17 P. Campinho, M. Behrndt, J. Ranft, T. Risler, N. Minc and C.-P. Heisenberg, *Nat. Cell Biol.*, 2013, **15**, 1405–1414.

18 H. Morita, S. Grigolon, M. Bock, S. F. G. Krens, G. Salbreux and C.-P. Heisenberg, *Dev. Cell*, 2017, **40**, 354–366.

19 A. Fruleux and A. Boudaoud, *Proc. Natl. Acad. Sci. U. S. A.*, 2019, **116**, 1940–1945.

20 O. K. Damavandi and D. K. Lubensky, *Proc. Natl. Acad. Sci. U. S. A.*, 2019, **116**, 5350–5355.

21 A. Jurado, J. Isensee, A. Hofemeier, L. J. Krüger, R. Wittkowski, R. Golestanian, P. Bittihn and T. Betz, 3D Dynamic Multiscale Force and Shape Analysis of In-Vivo Elastic Stress Sensors, *bioRxiv*, 2025, preprint, DOI: 10.1101/2025.01.22.633835v3.

22 B. I. Shraiman, *Proc. Natl. Acad. Sci. U. S. A.*, 2005, **102**, 3318–3323.

23 M. Basan, J. Prost, J.-F. Joanny and J. Elgeti, *Phys. Biol.*, 2011, **8**, 026014.

24 Y. G. Pollack, P. Bittihn and R. Golestanian, *New J. Phys.*, 2022, **24**, 073003.

25 L. Hupe, Y. G. Pollack, J. Isensee, A. Amiri, R. Golestanian and P. Bittihn, A Minimal Model of Smoothly Dividing Disk-Shaped Cells, *arXiv*, 2024, preprint, arXiv:2409.01959, DOI: 10.48550/arXiv.2409.01959.

26 S. X. Sun and H. Jiang, *Microbiol. Mol. Biol. Rev.*, 2011, **75**, 543–565.

27 J. Zimmerberg and M. M. Kozlov, *Nat. Rev. Mol. Cell Biol.*, 2006, **7**, 9–19.

28 R. C. Cail and D. G. Drubin, *Trends Cell Biol.*, 2023, **33**, 427–441.

29 E. C. Garner, *Annu. Rev. Cell Dev. Biol.*, 2021, **37**, 1–21.

30 N. van den Berg, K. Thijssen, T. T. Nguyen, A. Sarlet, M. Cordero, A. G. Vázquez, N. Mitarai, A. Doostmohammadi and L. Jauffred, Emergent Collective Alignment Gives Competitive Advantage to Longer Cells during Range Expansion, *bioRxiv*, 2024, preprint, DOI: 10.1101/2024.01.26.577059v4.

31 F. Chang and K. C. Huang, *BMC Biol.*, 2014, **12**, 54.

32 C. Billaudeau, A. Chastanet, Z. Yao, C. Cornilleau, N. Mirouze, V. Fromion and R. Carballido-López, *Nat. Commun.*, 2017, **8**, 15370.

33 Z. You, D. J. G. Pearce, A. Sengupta and L. Giomi, *Phys. Rev. X*, 2018, **8**, 031065.

34 D. Boyer, W. Mather, O. Mondragón-Palomino, S. Orozco-Fuentes, T. Danino, J. Hasty and L. S. Tsimring, *Phys. Biol.*, 2011, **8**, 026008.

35 D. Volfson, S. Cookson, J. Hasty and L. S. Tsimring, *Proc. Natl. Acad. Sci. U. S. A.*, 2008, **105**, 15346–15351.

36 D. Dell'Arciprete, M. L. Blow, A. T. Brown, F. D. C. Farrell, J. S. Lintuvuori, A. F. McVey, D. Marenduzzo and W. C. K. Poon, *Nat. Commun.*, 2018, **9**, 4190.

37 S. Orozco-Fuentes and D. Boyer, *Phys. Rev. E: Stat., Nonlinear, Soft Matter Phys.*, 2013, **88**, 012715.

38 R. Wittmann, G. H. P. Nguyen, H. Löwen, F. J. Schwarzendahl and A. Sengupta, *Commun. Phys.*, 2023, **6**, 1–13.

39 G. T. Fortune, N. M. Oliveira and R. E. Goldstein, *Phys. Rev. Lett.*, 2022, **128**, 178102.

40 M. Basaran, Y. I. Yaman, T. C. Yüce, R. Vetter and A. Kocabas, *eLife*, 2022, **11**, e72187.

41 P. Bittihn, A. Didovyk, L. S. Tsimring and J. Hasty, *Nat. Microbiol.*, 2020, **5**, 697–705.

42 J. Isensee, L. Hupe, R. Golestanian and P. Bittihn, *J. R. Soc., Interface*, 2022, **19**, 20220512.

43 Z. You, D. J. G. Pearce and L. Giomi, *Sci. Adv.*, 2021, **7**, eabc8685.

44 F. D. C. Farrell, O. Hallatschek, D. Marenduzzo and B. Waclaw, *Phys. Rev. Lett.*, 2013, **111**, 168101.

45 B. Langeslay and G. Juarez, *Soft Matter*, 2024, **20**, 8468–8479.

46 B. Langeslay, W. Fahy and G. Juarez, *Phys. Rev. E*, 2024, **109**, 054608.

47 B. Langeslay and G. Juarez, *Soft Matter*, 2023, **19**, 3605–3613.

48 L. Onsager, *Ann. N. Y. Acad. Sci.*, 1949, **51**, 627–659.

49 M. Doi, S. F. Edwards and S. F. Edwards, *The Theory of Polymer Dynamics*, Clarendon Press, 1988.

50 P. G. D. Gennes and J. Prost, *The Physics of Liquid Crystals*, Oxford University PressOxford, 1993.

51 F. M. Leslie, *Arch. Ration. Mech. Anal.*, 1968, **28**, 265–283.

52 J. L. Ericksen, *J. Rheol.*, 1961, **5**, 23–34.

53 N. J. Mottram and C. J. P. Newton, Introduction to Q-tensor Theory, *arXiv*, 2014, preprint, arXiv:1409.3542, DOI: 10.48550/arXiv.1409.3542.

54 C. W. Oseen, *J. Chem. Soc., Faraday Trans.*, 1933, **29**, 883–899.

55 F. C. Frank, *Faraday Discuss.*, 1958, **25**, 19–28.

56 Y. I. Yaman, E. Demir, R. Vetter and A. Kocabas, *Nat. Commun.*, 2019, **10**, 2285.

57 A. Doostmohammadi, J. Ignés-Mullol, J. M. Yeomans and F. Sagués, *Nat. Commun.*, 2018, **9**, 3246.

58 A. Doostmohammadi, S. P. Thampi and J. M. Yeomans, *Phys. Rev. Lett.*, 2016, **117**, 048102.

59 K. Copenhagen, R. Alert, N. S. Wingreen and J. W. Shaevitz, *Nat. Phys.*, 2021, **17**, 211–215.

60 L. Hupe, J. Isensee and P. Bittihn, *InPartS: Interacting Particle Simulations in Julia*, InPartS.org, 2022, https://hdl.handle.net/21.11101/0000-0007-FE12-7.

61 D. A. King and R. D. Kamien, *Phys. Rev. E*, 2023, **107**, 064702.

62 J. Bezanson, A. Edelman, S. Karpinski and V. Shah, *SIAM Rev.*, 2017, **59**, 65–98.

63 S. Danisch and J. Krumbiegel, *J. Open Source Softw.*, 2021, **6**, 3349.